JACS
JOURNAL OF THE AMERICAN CHEMICAL SOCIETY
pubs.acs.org/JACS
Article

Electrochemical Anion Sensing Using Conductive Metal−Organic Framework Nanocrystals with Confined Pores

Jiawei Huang, Audrey M. Davenport, Kelsie Heffernan, Tekalign T. Debela, Checkers R. Marshall, Jacob McKenzie, Meikun Shen, Shujin Hou, James B. Mitchell, Kasinath Ojha, Christopher H. Hendon, and Carl K. Brozek*

Cite This: https://doi.org/10.1021/jacs.4c06669

ABSTRACT: Anion sensing technology is motivated by the widespread and critical roles played by anions in biological systems and the environment. Electrochemical approaches comprise a major portion of this field but so far have relied on redox-active molecules appended to electrodes that often lack the ability to produce mixtures of distinct signatures from mixtures of different anions. Here, nanocrystalline films of the conductive metal−organic framework (MOF) Cr(1,2,3-triazolate)$_2$ are used to differentiate anions based on size, which consequently affect the reversible oxidation of the MOF. During framework oxidation, the intercalation of larger charge-balancing anions (e.g., ClO_4^-, PF_6^-, and OTf^-) gives rise to redox potentials shifted anodically by hundreds of mV due to the additional work of solvent reorganization and anion desolvation. Smaller anions (e.g., BF_4^-) may enter partially solvated, while larger ansions (e.g., OTf^-) intercalate with complete desolvation. As a proof-of-concept, we leverage this "nanoconfinement" approach to report an electrochemical ClO_4^- sensor in aqueous media that is recyclable, reusable, and sensitive to sub-100-nM concentrations. Taken together, these results exemplify an unusual combination of distinct external versus internal surface chemistry in MOF nanocrystals and the interfacial chemistry they enable as a novel supramolecular approach for redox voltammetric anion sensing.

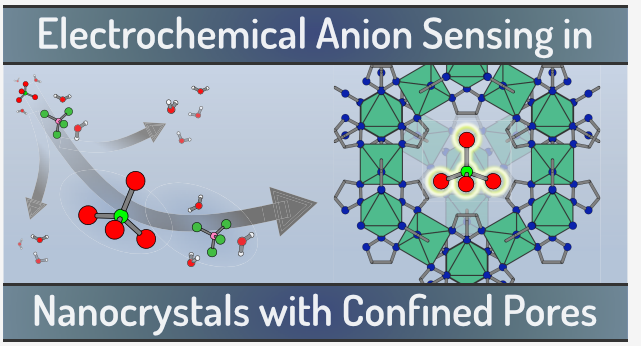

INTRODUCTION

Anions serve diverse and important roles in biological,[1,2] electrochemical,[3−7] and environmental systems.[8−10] Their impacts on health are critical and may be either beneficial or acutely toxic. For example, NO_3^- is a major component of agricultural fertilizer, but it also spawns algae blooms that endanger marine wildlife and access to safe drinking water.[11−13] These fertilizer sources often also introduce ClO_4^-, which is highly soluble and stable in water and which disrupts the healthy function of thyroids by blocking I^- transport.[14−16] Myriad technologies have been developed, therefore, to detect and differentiate anions in biological and environmental media. Fluorescent, colorimetric, anion-responsive gel, and electrochemical materials comprise most anion sensors, where selective supramolecular guest−host interactions trigger on−off material behavior, such as turn-on fluorescence or voltammetric shifts to redox potentials.[17−19] Among these technologies, electrochemical anion sensing attracts intense interest due to its inherent affordability, sensitivity, and scalability, with commercial products capable of nanomolar detection.[20] However, most electrochemical anion sensors function only in nonpolar organic solvents. In addition, analyzing mixtures of anions, such as those found in biological and environmental samples, poses considerable challenges. Selective adsorption of certain ions can block access from other anions, while detecting mixtures of signals from mixtures of anions remains an outstanding challenge.

Supramolecular chemistry governs the guest−host interactions of electrochemical anion sensing technologies.[20−23] Finely tuned van der Waals, secondary bonding, and other noncovalent interactions have been engineered into the sensor molecules that functionalize electrode surfaces. However, this approach suffers from the water instability of most sensor molecules, and it lacks control over the long-range supramolecular chemistry of the electrode−analyte interface. Extended solids with intrinsic conductivity and redox-active sites offer a potential alternative. Due to their well-ordered porous structures, ultrahigh surface areas, synthetic tunability, and compositional diversity,[24−26] metal−organic frameworks

Received: May 15, 2024
Revised: July 5, 2024
Accepted: July 8, 2024
Published: July 16, 2024

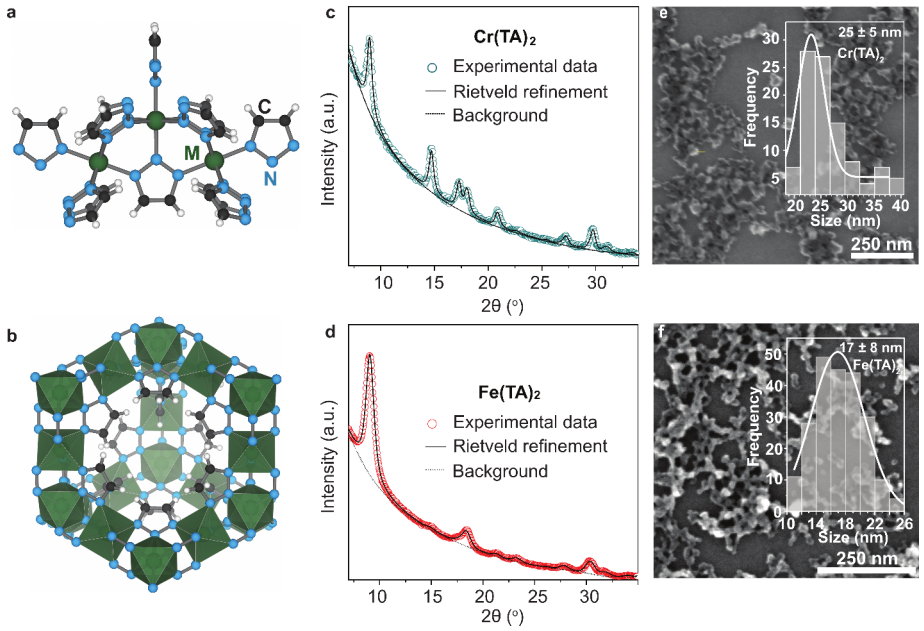

Figure 1. $Cr(TA)_2$ and $Fe(TA)_2$ nanoparticles. (a) Secondary building unit (SBU) cluster of $M(TA)_2$, M = Fe or Cr. (b) Idealized representation of Cr/$Fe(TA)_2$ pore structure based on the bulk crystalline structure. PXRD patterns and Rietveld refinement fittings for (c) $Cr(TA)_2$ and (d) $Fe(TA)_2$ nanoparticles. SEM images of (e) 25 nm $Cr(TA)_2$ and (f)17 nm $Fe(TA)_2$ nanoparticles.

(MOFs) achieve state-of-the-art performance in technologies based on guest−host chemistry, including carbon capture,[27−30] chemical separations,[31−34] ion transport,[35−39] and water harvesting from dry air.[40,41] Conductive MOFs[42] have found widespread applications as sensors leveraging chemiresistive,[43−45] fluorescent,[46−49] or colorimetric behavior.[50] A recent report even suggests conductive MOFs may produce mixtures of voltammetric signals from mixtures of analytes, although the underlying mechanism has yet to be elucidated.[51] Recent studies of conductive MOF nanoparticles (nanoMOFs) of Fe(1,2,3-triazolate)$_2$ ($Fe(TA)_2$) demonstrated significantly enhanced solution processability of nanoMOFs into functionalized electrodes compared to bulk powder.[52] These studies also revealed that the 4.5 Å pore apertures of $Fe(TA)_2$ caused the redox potential of interior Fe sites to anodically shift over 1.2 V compared to the oxidation of external Fe sites due to the energetics of solvent reorganization and BF_4^- desolvation, whereas intercalation of the larger anions PF_6^- and ClO_4^- was blocked entirely. As a result, we could not fully explore the impact of electrolyte ion size on the thermodynamics, kinetics, and mass transport processes governing ion intercalation redox chemistry within $Fe(TA)_2$ nanoMOFs and its practical applications. We hypothesized that thin films of conductive nanoMOFs with larger pores would permit redox intercalation of larger anions but at distinct thermodynamic potentials owing to anion-specific sterics and desolvation processes. Redox-active thin film electrodes with such nanoconfined pores could allow reversible electrochemical detection of mixed-analyte solutions at potentials specific to anion size and solvation and redox intercalation energetics.

Among the family of $M(TA)_2$ materials originally reported as bulk material,[53−56] only $Cr(TA)_2$ and $Fe(TA)_2$ were both redox-active and electrically conductive. In our attempts to nanosize this family of materials, we successfully prepared $Zn(TA)_2$ and $Cd(TA)_2$ nanoparticles but found them to be electronic insulators and lacking in redox activity (Figure S1). Although its single-crystal structure is not known, DFT calculations suggest, as detailed below, that $Cr(TA)_2$ possesses larger pore apertures compared to $Fe(TA)_2$, which is consistent with the structure determined by powder X-ray diffraction reported by Long et al.[55] Here, we report electrochemical anion sensors based on conductive thin films of porous $Cr(TA)_2$ nanocrystals (Figures 1a,b) capable of detecting mixtures of anions as distinct, reversible, and reproducible voltammetric signals separated by hundreds of millivolts. The $Cr(TA)_2$ sensors operate under aqueous conditions and repeated cycling with nanomolar detection limits. On a fundamental level, the sensing mechanism involves a redox-coupled anion intercalation process sensitive to the anion size, desolvation and redox intercalation thermodynamics, offering a distinct form of supramolecular chemistry for designing advanced sensor technologies.

RESULTS AND DISCUSSION

The synthesis of $Cr(TA)_2$ and $Fe(TA)_2$ nanoparticles followed the previously reported routes, where 1-methylimidazole (1-mIm) functioned as a "modulator" to reduce particle sizes below 100 nm.[53−55] Powder X-ray diffraction (PXRD) patterns confirm that the crystallites possess the expected crystal structures of low-spin $Cr(TA)_2$ and $Fe(TA)_2$ phases (Figure 1c,d). Scanning electron microscopy (SEM) analysis indicate average nanoparticle size of ca. 25 nm for $Cr(TA)_2$ and 17 nm for $Fe(TA)_2$, respectively (Figure 1e,f). A previous study reported that triflate (OTf^-) anions from the $Cr(OTf)_2$ precursor remain inside the pores of bulk $Cr(TA)_2$ even after extensive washing procedures.[55] Accordingly, we conducted X-ray photoelectron spectroscopy (XPS) on the as-prepared $Cr(TA)_2$ nanocrystals and detected a sulfur (S) signal from OTf^- anions (Figure S2). Further XPS analysis shows that the ratio of Cr/S approaches ca. 1:1, much higher than the reported value (i.e., 1:0.33) in bulk $Cr(TA)_2$.[55] We hypothesize that distinct from bulk where OTf^- anions mainly exist within the pores, nanosizing $Cr(TA)_2$ crystals significantly increases the external surface area and allows for the

https://doi.org/10.1021/jacs.4c06669
J. Am. Chem. Soc. XXXX, XXX, XXX−XXX

adsorption of additional OTf^- to external surface defects. Similarly, the chloride (Cl) XPS feature from $FeCl_2$ precursors is also evident in as-prepared $Fe(TA)_2$ nanocrystals, suggesting the existence of Cl^- anions within the nanopores (Figure S3). Nevertheless, Rietveld refinement performed from an idealized $Fe(TA)_2$ crystal model without the inclusion of Cl^- anions produced a good match with the experimental XRD patterns (Figure S4 and additional discussion in SI).

Due to the difficulty of probing MOF nanocrystal internal pores by experimental methods, density functional theory (DFT) calculations were performed for atomic-level insights into the local pore environments. As shown in Figure S5a, DFT-computed structures indicate distances of C−C and H−H are 11.5 and 3.4 Å, respectively, inside $Fe(TA)_2$ nanopores, respectively. By comparison, DFT results show that OTf^- anions inside $Cr(TA)_2$ nanopores lead to a larger pore as evidenced by an extension of the C−C and H−H distances to 12.1 and 3.8 Å, respectively (Figure S5b).

Redox-Induced Anion Intercalation within $Cr(TA)_2$ and $Fe(TA)_2$ Nanocrystals. To understand the impact of pore size on redox intercalation energetics, nanoparticle thin films of $Fe(TA)_2$ and $Cr(TA)_2$ were investigated by cyclic voltammetry. As shown in Figure 2a, the BF_4^--intercalation-induced $Fe^{2+/3+}$ chemistry of $Fe(TA)_2$ nanocrystal films exhibits a notably sharp and reversible redox feature at ca. 1.2 V vs $Fc^{0/+}$, as reported previously.[52] Because solvated BF_4^- anions (diameter of ca. 10 Å) exceed the ca. 3.4 Å pore diameter of the $Fe(TA)_2$ nanopore (i.e., as defined by the H−H distance in Figure S5a), the large potential of 1.2 V vs $Fc^{0/+}$ originates from the additional driving force for complete desolvation and intercalation of bare BF_4^- anions (diameter of ca. 3 Å).[52] Surprisingly, the sharp and reversible redox feature cathodically shifts to ca. −0.6 V vs $Fc^{0/+}$ in $Cr(TA)_2$ nanocrystal films (green curve in Figure 2a). Scan-rate-dependent CV studies indicate that the current density of this −0.6 V voltammetric feature relates to the squared root of scan rate (Figure S6a), identifying the origin of this redox feature as a diffusion-controlled process (see Figure S6b for additional data and discussions about scan-rate-dependent CV studies into surface Cr redox feature). *In situ* electrochemical quartz crystal microbalance (EQCM) electrodes also detected a significant mass increase at the −0.6 V redox peak (Figure S7), further associating this redox feature with the mass transport of BF_4^- anions into the $Cr(TA)_2$ nanocrystal pores. Cycling the scans causes both current and mass-to-charge ratio changes to increase progressively until ca. 20 scans (Figure S8). During this cycling, the redox peak cathodically shifts ca. 50 mV, suggesting that redox intercalation becomes more favorable. This result suggests that the $Cr(TA)_2$ films require a conditioning period, likely due to the need for native OTF^- to be removed for maximum BF_4^- intercalation (see Supporting Information for additional details). Overall, the significant cathodic shift of the BF_4^- intercalation redox feature from ca. 1.2 V vs $Fc^{0/+}$ in $Fe(TA)_2$ to ca. −0.6 V vs $Fc^{0/+}$ in $Cr(TA)_2$ nanoparticle film suggests much more favorable transport of BF_4^- anions into the pores of $Cr(TA)_2$ nanocrystals.

Analysis of the differing CV peak shapes for the Fe and Cr materials provides insight into mechanistic differences between the two intercalation processes. Specifically, whereas the feature at ca. 1.2 V vs $Fc^{0/+}$ in $Fe(TA)_2$ consists of a prewave (i.e., in the potential range of ca. 1.0−1.2 V vs $Fc^{0/+}$) and a sharp peak, only a sharp feature exists for $Cr(TA)_2$ at ca. −0.6 V vs $Fc^{0/+}$ (Figure 2a). The prewave observed with $Fe(TA)_2$

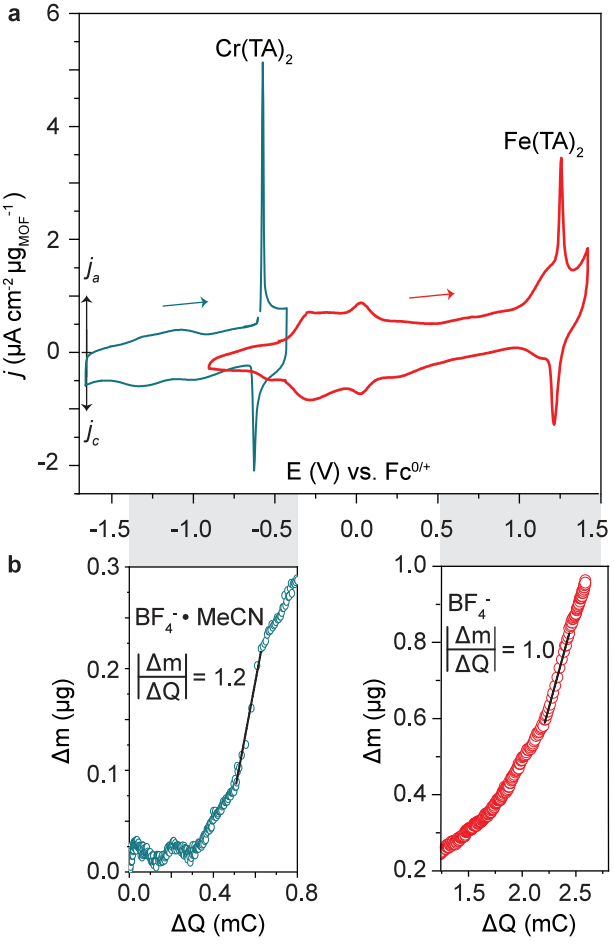

Figure 2. EQCM studies of $Cr(TA)_2$ and $Fe(TA)_2$ films. (a) CV traces of $Cr(TA)_2$ and $Fe(TA)_2$ nanoparticle films. (b) Mass change vs charge change in $Cr(TA)_2$ and $Fe(TA)_2$ films during CV measurements. The black line represents the potential region for BF_4^--intercalation-induced redox inside the nanopores of $Cr(TA)_2$ and $Fe(TA)_2$ nanocrystals. Only the mass change vs charge change in the anodic scan direction is shown. Note: CV traces and mass-to-charge ratio are collected using EQCM electrodes and 0.1 M tetrabutylammonium tetrafluoroborate ($TBABF_4$) as electrolyte in acetonitrile. The spin-coating amount of 17 nm $Fe(TA)_2$ nanoparticles onto the EQCM crystal is ca. 4.0 μg, and the spin-coating amount of 25 nm $Cr(TA)_2$ nanoparticles onto the EQCM crystal is ca. 3.4 μg. CV is collected at a 10 mV/s scan rate.

was assigned previously to adsorption and desolvation of BF_4^- anions prior to intercalation into the nanoconfined pores.[52] Accordingly, the absence of a prewave for the $Cr(TA)_2$ nanoparticle film indicates that BF_4^- anions intercalate without complete desolvation. To investigate interfacial BF_4^- transfer further, we monitored the mass and charge changes at the intercalation redox events for both $Cr(TA)_2$ and $Fe(TA)_2$ nanoparticle films using *in situ* EQCM. Previous studies reported that the apparent molecular mass (M_w') of a species can be measured by eq 1:

$$M_w' = zF\left(\frac{\Delta m}{\Delta Q}\right) \quad (1)$$

where z represents the number of electrons and F is Faraday's constant. From M_w', the solvation number (n) of BF_4^- anions involved during the intercalation/de-intercalation process can be determined via eq 2:

https://doi.org/10.1021/jacs.4c06669
J. Am. Chem. Soc. XXXX, XXX, XXX−XXX

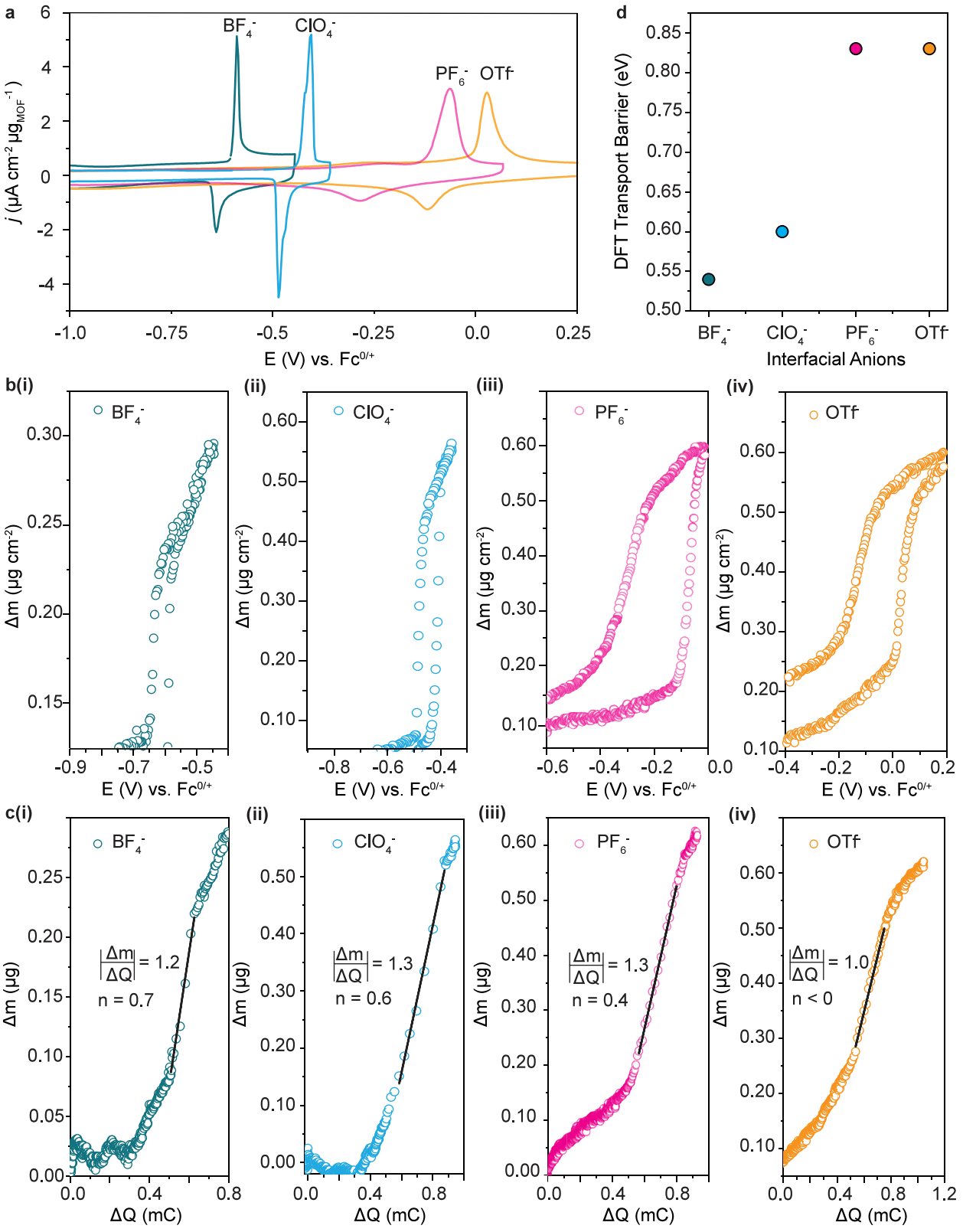

Figure 3. Anion-dependent intercalation redox chemistry inside $Cr(TA)_2$ nanopores. (a) Anion-dependent CV measurements of $Cr(TA)_2$ nanoparticle films. (b) Mass change of a $Cr(TA)_2$ film in the potential region of intercalation redox with (i) BF_4^-, (ii) ClO_4^-, (iii) PF_6^-, and (iv) OTf^-. (c) Mass-to-charge ratio at the intercalation redox event with (i) BF_4^-, (ii) ClO_4^-, (iii) PF_6^-, and (iv) OTf^- into a $Cr(TA)_2$ film. (d) DFT calculation of anion transport energy inside $Cr(TA)_2$ nanopores Note: CV traces, mass variation, and mass-to-charge ratio are all collected using EQCM electrodes and 0.1 M electrolytes in acetonitrile. The spin-coating amount of 25 nm $Cr(TA)_2$ nanoparticles onto EQCM crystal is ca. 3−4 μg. CV is collected at a 10 mV/s scan rate.

https://doi.org/10.1021/jacs.4c06669
J. Am. Chem. Soc. XXXX, XXX, XXX−XXX

$$n = \frac{M_w' - M_w(BF_4^-)}{M_w(\text{solvent})} \quad (2)$$

where $M_w(BF_4^-)$ denotes the molecular weight of BF_4^- anions and M_w(solvent) is the molecular weight of solvent (e.g., acetonitrile).[57−59] If the BF_4^- anions intercalate into either $Cr(TA)_2$ or $Fe(TA)_2$ nanopores without a solvation shell, the theoretical slope of $\frac{\Delta m}{\Delta Q}$ should be ca. 0.9 (i.e., obtained under the assumption of $n = 0$ and $M_w' = M_w(BF_4^-)$). As shown in Figure 2b, the slope of $\frac{\Delta m}{\Delta Q}$ (ca. 1.0) at the intercalation feature of $Fe(TA)_2$ nanocrystals approaches the theoretical value expected for the complete desolvation process. By contrast for $Cr(TA)_2$, we observed a $\frac{\Delta m}{\Delta Q}$ slope of ca. 1.2 (see Figures 2b and S7 for the mass change on $Cr(TA)_2$ film during CV measurements). This $\frac{\Delta m}{\Delta Q}$ value exceeds the theoretical value of complete desolvation (i.e., ca. 0.9), indicating that BF_4^- anions transfer into nanopores with acetonitrile molecules (i.e., a partial desolvation interfacial transfer mechanism) and therefore $Cr(TA)_2$ nanocrystals possess larger nanopores as compared to $Fe(TA)_2$. Furthermore, DFT calculations using the climbing image nudged elastic band (CI-NEB) method determined an energetic barrier of 0.54 eV for BF_4^- anions transporting between the nanopores of $Cr(TA)_2$ (Figure S10), compared to a larger barrier of ca. 0.84 eV for $Fe(TA)_2$.[52] Inspired by prior work of using vibrational spectroscopy to probe dynamic bonding environments within MOFs under external stimulus,[60,61] $Cr(TA)_2$ and $Fe(TA)_2$ nanoparticle thin films were monitored by in operando Raman spectroscopy under the relevant electrochemical conditions (Figure S11 and see Supporting Information for additional details). The far greater red shift of the slope of the $Cr(TA)_2$ triazolate vibrational modes compared to that of $Fe(TA)_2$ (31 cm^{-1}/V vs 13 cm^{-1}/V) suggests greater bond flexibility in the Cr system, which may facilitate the intercalation process. These EQCM, theoretical, and spectroscopic results demonstrate that the pore enlargement further reduces the gating effect on the entry of BF_4^- anions, resulting in a massive potential shift in the intercalation redox feature from ca. 1.2 V vs $Fc^{0/+}$ in $Fe(TA)_2$ to ca. −0.6 V vs $Fc^{0/+}$ in the $Cr(TA)_2$ nanocrystal film.

The surface redox peak for the $Fe(TA)_2$ film also shifts from 0 V vs $Fc^{0/+}$ to ca. −1.1 V vs $Fc^{0/+}$ for the $Cr(TA)_2$ film (Figure 2a). This 1.1 V cathodic shift observed for $Cr(TA)_2$ compared to $Fe(TA)_2$ originates from the more "active" low-spin Cr^{2+}/Cr^{3+} redox chemistry compared to the low-spin Fe^{2+}/Fe^{3+} redox activity. The 1.8 V shift observed in the intercalation redox peak between $Fe(TA)_2$ (1.2 V vs $Fc^{0/+}$) and $Cr(TA)_2$ (−0.6 V vs $Fc^{0/+}$) is therefore attributable to two factors: the difference in redox activity between Cr and Fe centers (ca. 1.1 V) and the nanoconfinement effect leading to differences in intercalation redox potential between the smaller $Fe(TA)_2$ pores and the larger $Cr(TA)_2$ pores (ca. 0.7 V). Notably, the 0.7 V shift due to pore size is significant in the context of electrochemistry. For example, a 180 mV difference in redox potentials between two molecules would result in an electron transfer between them going to 99.9% completion, based on the Nernst equation. This result highlights the crucial role of pore size in determining the thermodynamics of ion-intercalation redox chemistry within MOF nanopores.

Anion-Dependent Intercalation Redox Chemistry within $Cr(TA)_2$ Nanocrystals. To explore the impact of electrolyte identity in controlling the intercalation redox chemistry within the pore of $Cr(TA)_2$ nanoparticles, we substituted BF_4^- anions for larger anions ClO_4^-, PF_6^-, and OTf^-, while keeping bulky tetrabutylammonium (TBA^+) as the countercation due to its weaker ion pairing strength on influencing anion intercalation into $Cr(TA)_2$ nanopores than Li^+ cations (Figure S12). Figures 3a and S13 show a large anodic shift to the $E_{1/2}$ of the intercalation redox feature from ca. −0.6 V vs $Fc^{0/+}$ to ca. −0.1 V vs $Fc^{0/+}$ upon switching the anion identity from the smallest anion BF_4^- to increasingly larger ClO_4^-, PF_6^-, and OTf^-. Scan-rate-dependent CV studies indicate that the current density of these anion-dependent sharp voltammetric features all relate to the squared root of scan rate (Figure S14), identifying the origin of ClO_4^--, PF_6^--, and OTf^--induced redox features as a diffusion-controlled process. To further identify the origin of this anion-dependent intercalation redox behavior, we recorded $\frac{\Delta m}{\Delta Q}$ and the corresponding solvation number (n) when using each anion. Figure 3c exhibits a continuous decrease in the n value for larger-size anions. In particular, the n value becomes negative for the OTf^--intercalation-induced redox, suggesting that the transfer of OTf^- anions requires both the complete desolvation and removal of solvent molecules (i.e., acetonitrile) from the pores. Moreover, EQCM experiments reveal that the mass-change hysteresis during anion intercalation (mass increase) and de-intercalation (mass decrease) broadens with the use of larger anions, suggesting that mass transport dynamics become more sluggish with increasing anion size (Figure 3b). Such anion-size-dependent mass transport dynamics is further supported by the larger ΔE value of the intercalation redox feature with increasing the anion size (Figure S15). DFT CI-NEB calculations further revealed that the larger anions result in a higher transport energy barrier within $Cr(TA)_2$ nanopores (Figures 3d, S16, S17, and S18). For instance, the mass transport barrier increases from ca. 0.54 eV for BF_4^- to ca. 0.83 eV for the larger OTf^- anions. These anion-dependent variations in solvation shell and transport energy barrier together demonstrate that the use of larger anions intensifies the nanoconfinement effect within the $Cr(TA)_2$ pores, gating the interfacial anion transfer and therefore thermodynamically and kinetically disfavoring the interior anion-coupled redox chemistry. Scheme 1 depicts the difference in these processes, where the more favorable redox-coupled intercalation of BF_4^- involves a solvation shell, whereas the anodically shifted intercalation of OTf^- requires complete desolvation, greater solvent reorganization, and a larger redox entropy change. We

Scheme 1. Representation of $Cr(TA)_2$ Pores before (left) and after Oxidation-Induced Anion Intercalation (right)

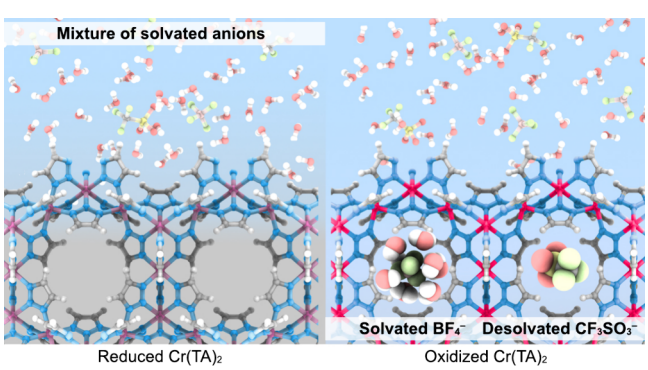

https://doi.org/10.1021/jacs.4c06669
J. Am. Chem. Soc. XXXX, XXX, XXX−XXX

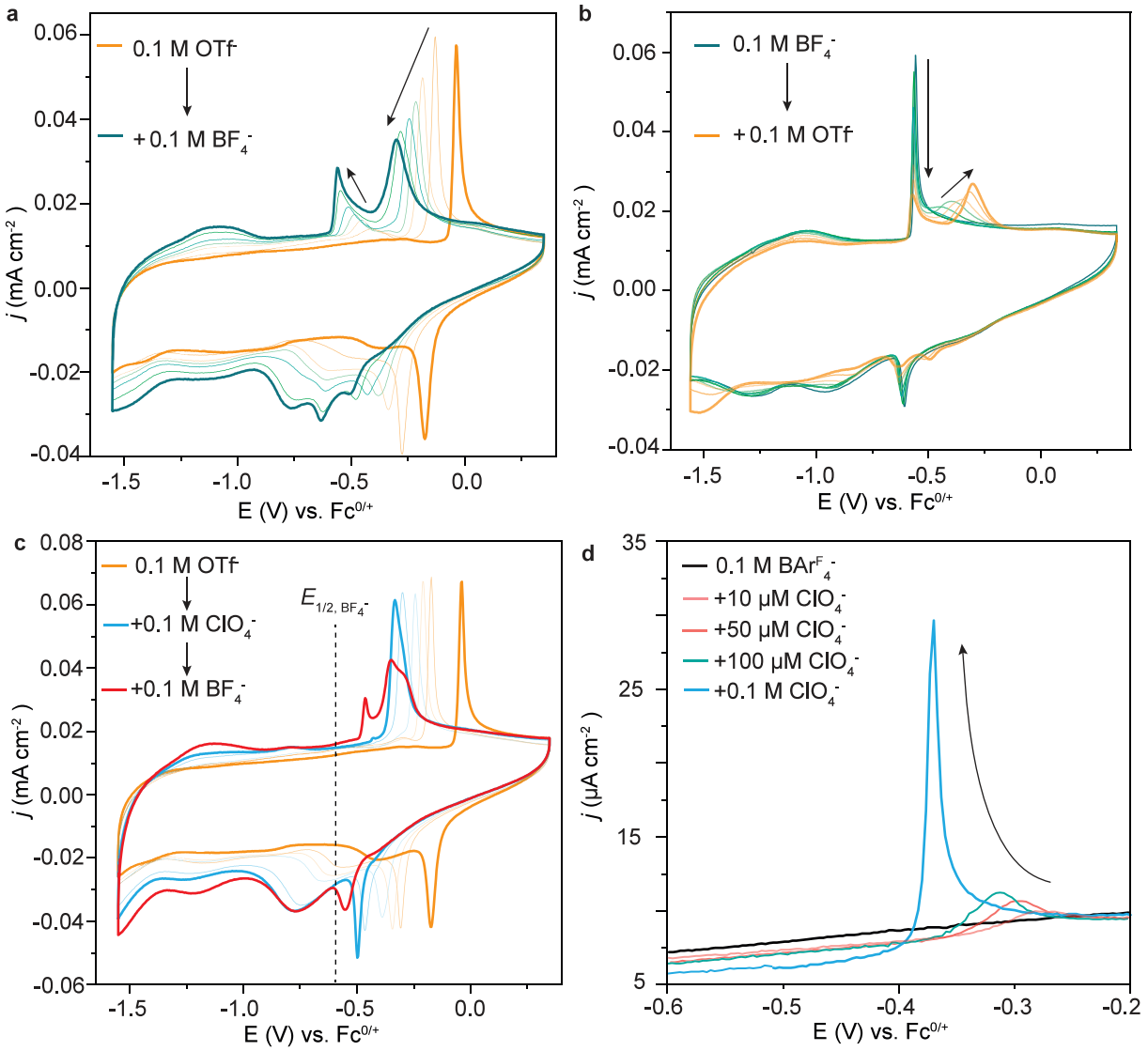

Figure 4. Intercalation redox chemistry of $Cr(TA)_2$ nanoparticle films in the presence of multiple anions. (a) CV measurements of a $Cr(TA)_2$ nanoparticle film during titration of $TBABF_4$ into a 0.1 M TBAOTf acetonitrile electrolyte. (b) CV measurements of a $Cr(TA)_2$ nanoparticle film during titration of TBAOTf into a 0.1 M $TBABF_4$ acetonitrile electrolyte. (c) CV measurements of a $Cr(TA)_2$ nanoparticle film during titration of both $TBABF_4$ and $TBAClO_4$ into a 0.1 M TBAOTf acetonitrile electrolyte. (d) CV measurements of a $Cr(TA)_2$ nanoparticle film during titration of $TBAClO_4$ into a 0.1 M $NaBAr^F{}_4$ acetonitrile electrolyte. Note: CV traces are collected using $Cr(TA)_2$ nanoparticle films on glassy carbon electrodes. CV is collected at a 10 mV/s scan rate.

also noticed that the current density of the ClO_4^--transfer-induced Cr redox peak exhibits greater symmetry compared to other anions with similar structure and size (e.g., BF_4^-). This difference is likely due to the distinct guest−host interactions between oxygen-containing anions and fluoride-containing anions during their intercalation and de-intercalation processes inside $Cr(TA)_2$ nanocrystals.

To investigate whether mixtures of signals could be detected from mixtures of anions, small quantities of $TBABF_4$ (i.e., mM scale) were titrated into a 0.1 M TBAOTf acetonitrile solution containing a 25 nm $Cr(TA)_2$ nanoparticle film. Figures 4a and S19a show that the addition of BF_4^- anions results in a new redox feature cathodically shifted from ca. −0.46 V vs $Fc^{0/+}$ to ca. −0.6 V vs $Fc^{0/+}$ as the concentration of BF_4^- anions increases from 1.5 mM to 0.1 M (see additional discussions about electrochemical titration studies in SI). The consistency of this −0.6 V feature after titration of 0.1 M $TBABF_4$ with the $E_{1/2}$ in pure $TBABF_4$, along with its BF_4^--concentration-dependent current density, clearly demonstrate that the new redox feature originates from interfacial BF_4^- transfer. Interestingly, the redox signature observed at ca. −0.1 V vs $Fc^{0/+}$ in pure OTf^- shifts to −0.4 V vs $Fc^{0/+}$ after the addition of 0.1 M BF_4^- (Figures 4a and S19b). This result suggests that the presence of BF_4^- promotes the OTf^- intercalation redox chemistry within $Cr(TA)_2$ nanoparticles. Based on the above *in situ* electrochemical Raman studies, we hypothesize that intercalated BF_4^- anions promote a structural distortion inside $Cr(TA)_2$ nanocrystals that enhances subsequent intercalation of OTf^- anions. As a control, we observed that the $E_{1/2}$ position of the BF_4^- intercalation redox feature at ca. −0.6 V vs $Fc^{0/+}$ remains unchanged when titrating TBAOTf into a 0.1 M $TBABF_4$ solution (Figure 4b). This result suggests that the initial presence of BF_4^- determines the local pore environment and it remains unchanged in the presence of OTf^- anions,

https://doi.org/10.1021/jacs.4c06669
J. Am. Chem. Soc. XXXX, XXX, XXX−XXX

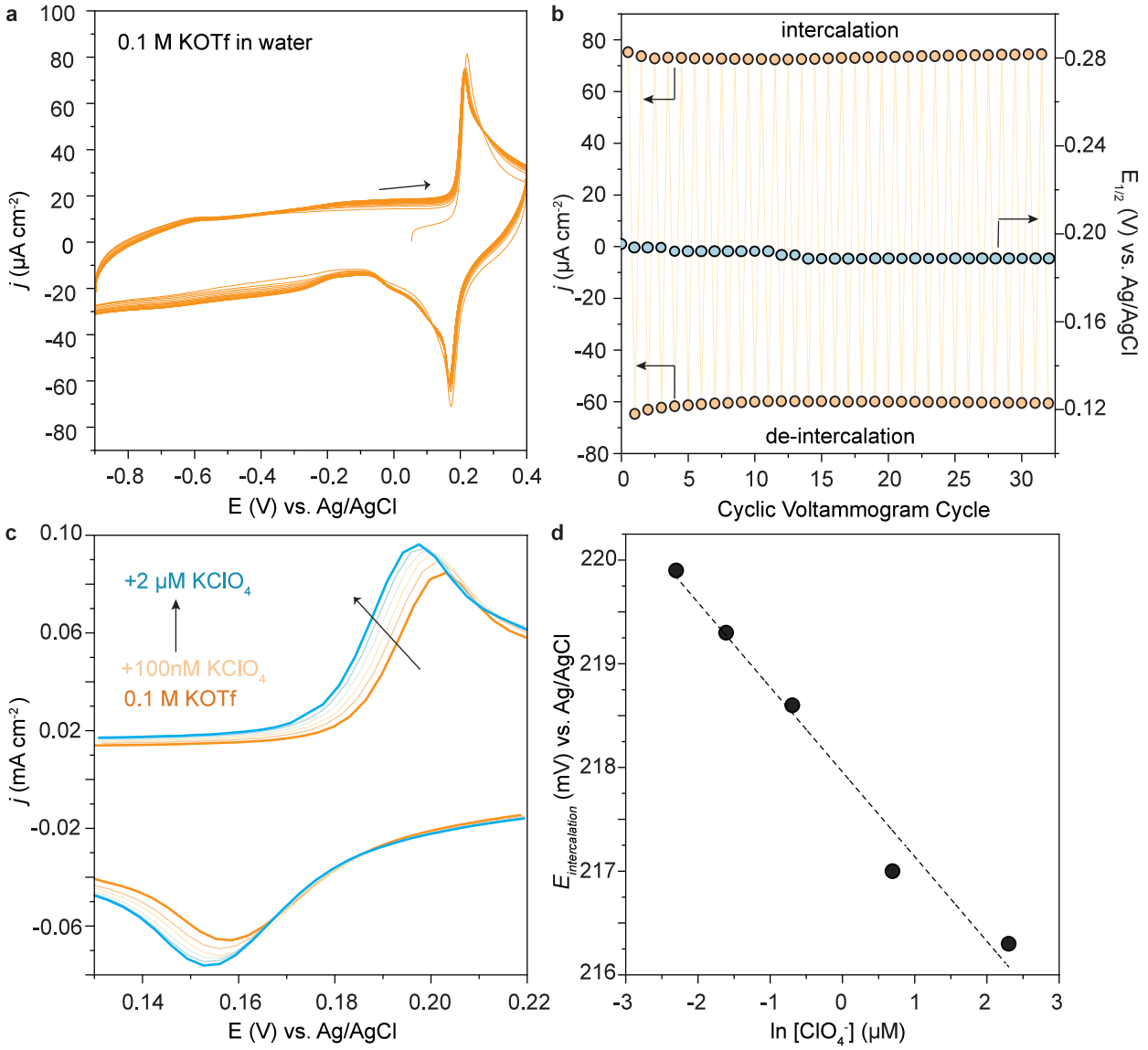

Figure 5. Anion sensing using $Cr(TA)_2$ nanocrystals in aqueous media. (a) Structural stability test of $Cr(TA)_2$ nanoparticle film in water via multiple CV measurement cycles. (b) Trace-dependent $E_{1/2}$ of the intercalation redox feature and trace-dependent current density of the intercalation and de-intercalation redox feature. (c) Sensing of ClO_4^- anions using a $Cr(TA)_2$ nanoparticle film in aqueous solution by CV measurements and (d) the variation of $E_{1/2}$ for the intercalation redox feature during titrations of $KClO_4$ into a 0.1M KOTf aqueous electrolyte solution. Note: CV traces were collected using $Cr(TA)_2$ nanoparticle films on glassy carbon electrodes. CV traces were collected at a 10 mV/s scan rate. Potassium cations are used as countercations during anion-dependent titration experiments.

leading to the OTf^--titration-independent $E_{1/2}$ value for the BF_4^- intercalation redox feature.

To explore the possibility of detecting mixtures with three anions, two subsequent titrations were performed. First, $TBAClO_4$ was titrated into a 0.1 M TBAOTf electrolyte solution. As shown in Figures 4c, S20, and S21, the presence of ClO_4^- introduces a distinct redox feature and a cathodic shift to the OTf^- intercalation redox feature. At ClO_4^- concentrations of 0.1 M, the ClO_4^- and OTf^- redox intercalation peaks merge into a single broad feature with an $E_{1/2}$ value of ca. −0.4 V vs $Fc^{0/+}$. These results suggest that the presence of ClO_4^- and the structural changes it induces to the MOF pore cause the redox intercalation of ClO_4^- and OTf^- anions to become electrochemically similar. Interestingly, titrating 0.1 M BF_4^- anions, as a third component, into a 0.1 M TBAOTf and 0.1 M $TBAClO_4$ electrolyte solution induces another distinct redox feature at −0.5 V vs $Fc^{0/+}$ (Figure 4c) The observed $E_{1/2}$ value differs from the −0.6 V vs $Fc^{0/+}$ feature observed for pure BF_4^- solutions. We attribute this difference to the interaction of the three distinct anions disfavoring the transport of BF_4^- anions into $Cr(TA)_2$ pores. Interestingly, the addition of BF_4^- anions decreases the current density of the ClO_4^-/OTf^- intercalation redox features and causes them to split into two distinct waves (Figure 4c). We propose that BF_4^- intercalation sufficiently alters the $Cr(TA)_2$ to facilitate ClO_4^- intercalation over OTf^-. This hypothesis is supported by the cathodic shift of the ClO_4^- intercalation redox feature from −0.33 V vs $Fc^{0/+}$ in a 0.1 M ClO_4^- and 0.1 M OTf^- electrolyte solution to −0.35 V vs $Fc^{0/+}$ after the additional titration of 0.1 M BF_4^- anions. Meanwhile, the $E_{1/2}$ of the OTf^- intercalation redox remains unchanged before and after the addition of BF_4^- anions. Taken together, these anion-dependent investigations

https://doi.org/10.1021/jacs.4c06669
J. Am. Chem. Soc. XXXX, XXX, XXX−XXX

indicate that the presence of one type of anion influences the microscopic mechanism and, hence, the electrochemical potential of intercalation for another anion.

These results suggest that each anion produces a unique redox intercalation feature resulting from supramolecular chemistry specific to the anion. To test this interpretation, titrations were performed starting from $[BAr^F_4]^-$ anions. Due to the large van der Waals diameter of ca. 16 Å in contrast to the $Cr(TA)_2$ pore aperture of 3.8 Å (i.e., as defined by the H−H distance in Figure S5b), a redox intercalation feature would only be expected upon introduction of sufficiently small anions. Indeed, the voltammetric response of 25 nm $Cr(TA)_2$ thin films in 0.1 M $BAr^F_4{}^-$ anions shows no redox intercalation response, whereas a feature appears upon titration of 10 μM ClO_4^- (Figure 4d). Increased concentrations cause a cathodic shift of the redox wave, suggesting that the intercalation energetics become more favorable. The higher concentration detection limit in the presence of $BAr^F_4{}^-$ suggests that although this bulkier anion does not intercalate, it discourages intercalation of smaller anions perhaps by blocking access to pores. Nevertheless, these results confirm that electrochemical sensing of anions by this approach involves a turn-on mechanism sensitive to the specific energetics of anions to enter MOF pores. If the mechanism depends on the availability of MOF pores to anions, then we surmise sub-nM detection limits should be possible with appropriate electrochemical equipment to measure such low current densities.

Electrochemical Anion Sensing in Aqueous Media. The anion-coupled redox intercalation chemistry of $Cr(TA)_2$ nanocrystal thin films provides a novel platform for designing supramolecular acceptors for electrochemical anion sensors in biologically and environmentally relevant conditions. The U.S. Environmental Protection Agency (EPA) classifies ClO_4^- as a leading pollutant threatening environmental and food safety. Figure S22 shows that the intercalation redox feature of the $Cr(TA)_2$ nanocrystal film in 0.1 M TBAOTf acetonitrile solution undergoes a cathodic shift in the presence of only 50 nM ClO_4^-. This ClO_4^--induced shift to $E_{1/2}$ may be reversed after poising the film at a potential of −1.5 V vs $Fc^{0/+}$ for 20 min to de-intercalate ClO_4^- anions from the pores (Figure S23). These tests confirm that the $Cr(TA)_2$ nanocrystal film is highly sensitive and reusable for electrochemical ClO_4^- sensing. In addition to organic solvents, $Cr(TA)_2$ nanoparticle films also exhibit remarkable structural stability in aqueous media, as evidenced by the stable $E_{1/2}$ position of the intercalation redox peak and its repeatable current densities during the long-term CV cycles in a 0.1 M KOTf aqueous solution even after one-month immersion in aqueous media (Figures 5a,b and S24, and see additional discussions in SI). This result holds significant implications for the practical applications of $Cr(TA)_2$ in the field of anion sensing in aqueous solutions. Additionally, given that water is typically found in the environment with a pH range of 6.5 to 8, we investigated the structural stability of $Cr(TA)_2$ nanoMOFs across this pH range in aqueous media. As demonstrated by PXRD results in Figure S25, the characteristic PXRD peak of $Cr(TA)_2$ at around 9° remains unchanged after 1 week of immersion in solutions with varying pH. This stability suggests that the structure of $Cr(TA)_2$ nanoMOFs is not significantly impacted by the typical pH range of natural water environments. Similar to the detection limit of ClO_4^- in acetonitrile solvent, the ClO_4^--induced shift is detectable upon adding 100 nM ClO_4^- to 0.1 M KOTf aqueous solutions (the linear detection range of ClO_4^- extends from 100 nM to 10 μM in aqueous media in Figure 5c). Moreover, Figure 5d exhibits a linear relationship between $E_{1/2}$ and $\ln[ClO_4^-]$, suggesting that the intercalation redox feature of $Cr(TA)_2$ follows a Nernstian response to the concentration of ClO_4^- anions in aqueous solution (i.e., $E_{1/2}$ (mV) = (−0.8 ± 0.07) $\ln[ClO_4^-]$). This relationship, consistent with the above titration experiments, confirms the active participation of ClO_4^- anions in the Cr redox chemistry of $Cr(TA)_2$ nanocrystals within the nanoconfined pores.

Commercially available ClO_4^- sensors often suffer from interference from halides (Cl^-, Br^-, I^-), nitrates, and other larger multivalent anions (SO_4^{2-}, PO_4^{3-}) in aqueous media. While the presence of ClO_4^- induces a distinct $E_{1/2}$ shift in the intercalation peak of the Cr redox feature, halide anions (Cl^-, Br^-, I^-) cause a gradual decrease in the current density of the $Cr(TA)_2$ intercalation peak only at concentrations exceeding 10−20 μM (Figures S26−S29). The lack of distinct and sharp redox features related to halide intercalation into Cr-MOF nanopores suggests that halide anions do not experience a gating effect within the $Cr(TA)_2$ nanopores, and therefore exterior and interior Cr redox sites are indistinguishable from each other. The halide-reduced current density of the intercalation redox feature inside Cr-MOF originates from the fast mass transport dynamics and the strong binding tendency of halide anions into the interior Cr active sites, poisoning interior Cr centers. Similarly, we did not observe the sharp and reversible redox feature from $Cr(TA)_2$ nanoMOFs induced by NO_3^- intercalation, suggesting that the NO_3^- anions will not influence the use of $Cr(TA)_2$ for ClO_4^- sensing (Figure S30). Larger multivalent anions, such as SO_4^{2-}, also lack a sharp redox feature akin to the intercalation Cr redox signatures described above (Figure S31). As compared to monovalent ions, multivalent ions possess higher interfacial desolvation energies and slower transport dynamics both at the material/electrolyte interface and inside the solid-state materials. Consequently, we propose that instead of participating in the intercalation redox chemistry, solvated sulfate and phosphate anions block the entry of $Cr(TA)_2$ nanopores and prevent the anion-intercalation-induced Cr redox chemistry (see additional results and discussions about using Cr redox chemistry of $Cr(TA)_2$ nanocrystals for other anion sensing in SI).

For other forms of anion sensors, measuring direct current at a fixed potential (I−V curves) becomes considerably more complex when the target solution contains over three different small anions. This complexity arises from all anions contributing to double-layer charging currents at specific applied potentials. Unlike conventional supramolecular sensors that rely on ion−host intercalation, our approach leverages the combined effects of nanoconfinement and ion-gating within the $Cr(TA)_2$ nanopores to achieve exceptional ClO_4^- sensing selectivity. This unique strategy leads to distinct cyclic voltammetry responses (i.e., anion-induced distinct $E_{1/2}$ shift in the intercalation peak of the Cr redox feature) for ClO_4^- compared to other anions.

CONCLUSION

In summary, we report a method of electrochemical anion sensing based on conductive films of nanoparticles with pore apertures comparable to anion diameters. Distinct from the previous reports of $Fe(TA)_2$ that intercalated BF_4^- anions only if fully desolvated, replacing Fe with Cr centers enables the

https://doi.org/10.1021/jacs.4c06669
J. Am. Chem. Soc. XXXX, XXX, XXX−XXX

intercalation of a wider range of anions (e.g., BF_4^-, ClO_4^-, PF_6^-, and OTf^-) due to its enlarged pores, as revealed by spectroscopic and theoretical evidence. Such an increase in the pore size permits partially solvated BF_4^- anions to intercalate at potentials shifted from ca. 1.2 V vs $Fc^{0/+}$ in $Fe(TA)_2$ to ca. −0.6 V vs $Fc^{0/+}$ in $Cr(TA)_2$. Moreover, the use of larger anions continuously increases the anion gating effect inside the nanoconfined $Cr(TA)_2$ pores, leading to the transition from solvated BF_4^- transfer to complete desolvation and intercalation of OTf^- anions, and an anodic shift of redox potentials by over 500 mV. We further utilize this anion-dependent redox chemistry inside $Cr(TA)_2$ pores to successfully sense ca. 100 nM ClO_4^- anions in aqueous solutions with month-long structural stability. Additionally, these sensors may be reused after applying a negative voltage to de-intercalate ClO_4^-. Our work represents the first instance of an anion sensor that can detect multiple anions simultaneously. We highlight the key advantages of Cr-nanoMOFs as a ClO_4^- sensor compared to commercially available options due to their superior selectivity (i.e., Cr-nanoMOFs show distinct cyclic voltammetry responses to different anions, leading to minimal interference during ClO_4^- sensing), structural stability of Cr-MOF in aqueous solution and therefore long product lifetime, sustainable recycling time, and low detection limit (see additional comparison and discussions about the advantage of $Cr(TA)_2$ sensor compared to commercially available options in the SI). Taken together, our studies provide a clear understanding of how the cooperation between pore environment and anions determines the nanoconfinement gating effect that controls interfacial ion-coupled redox processes, while positioning $Cr(TA)_2$ nanocrystals as a novel alternative for supramolecular transducers for redox voltammetric anion sensing.

■ ASSOCIATED CONTENT

Supporting Information

The Supporting Information is available free of charge at https://pubs.acs.org/doi/10.1021/jacs.4c06669.

Experimental details and additional data (PDF)

■ AUTHOR INFORMATION

Corresponding Author

Carl K. Brozek − *Department of Chemistry and Biochemistry, Material Science Institute, University of Oregon, Eugene, Oregon 97403, United States; Oregon Center for Electrochemistry, University of Oregon, Eugene, Oregon 97403, United States;* orcid.org/0000-0002-8014-7904; Email: cbrozek@uoregon.edu

Authors

Jiawei Huang − *Department of Chemistry and Biochemistry, Material Science Institute, University of Oregon, Eugene, Oregon 97403, United States; Oregon Center for Electrochemistry, University of Oregon, Eugene, Oregon 97403, United States;* orcid.org/0000-0002-5184-2510

Audrey M. Davenport − *Department of Chemistry and Biochemistry, Material Science Institute, University of Oregon, Eugene, Oregon 97403, United States*

Kelsie Heffernan − *Department of Chemistry and Biochemistry, Material Science Institute, University of Oregon, Eugene, Oregon 97403, United States*

Tekalign T. Debela − *Department of Chemistry and Biochemistry, Material Science Institute, University of Oregon, Eugene, Oregon 97403, United States;* orcid.org/0000-0003-4859-2597

Checkers R. Marshall − *Department of Chemistry and Biochemistry, Material Science Institute, University of Oregon, Eugene, Oregon 97403, United States*

Jacob McKenzie − *Department of Chemistry and Biochemistry, Material Science Institute, University of Oregon, Eugene, Oregon 97403, United States*

Meikun Shen − *Department of Chemistry and Biochemistry, Material Science Institute, University of Oregon, Eugene, Oregon 97403, United States; Oregon Center for Electrochemistry, University of Oregon, Eugene, Oregon 97403, United States;* orcid.org/0000-0001-8100-4115

Shujin Hou − *Department of Chemistry and Biochemistry, Material Science Institute, University of Oregon, Eugene, Oregon 97403, United States; Oregon Center for Electrochemistry, University of Oregon, Eugene, Oregon 97403, United States;* orcid.org/0000-0002-3633-2387

James B. Mitchell − *Department of Chemistry and Biochemistry, Material Science Institute, University of Oregon, Eugene, Oregon 97403, United States; Oregon Center for Electrochemistry, University of Oregon, Eugene, Oregon 97403, United States*

Kasinath Ojha − *Department of Chemistry and Biochemistry, Material Science Institute, University of Oregon, Eugene, Oregon 97403, United States; Oregon Center for Electrochemistry, University of Oregon, Eugene, Oregon 97403, United States*

Christopher H. Hendon − *Department of Chemistry and Biochemistry, Material Science Institute, University of Oregon, Eugene, Oregon 97403, United States; Oregon Center for Electrochemistry, University of Oregon, Eugene, Oregon 97403, United States;* orcid.org/0000-0002-7132-768X

Complete contact information is available at: https://pubs.acs.org/10.1021/jacs.4c06669

Notes

The authors declare no competing financial interest.

■ ACKNOWLEDGMENTS

The authors thank the Science Foundation through the Division of Materials Research for funding under grant nos. DMR-2114430 and DMR-1956403. M.S. gratefully acknowledges funding from the Department of Energy, Basic Energy Sciences, award no. DESC0014279. J.B.M. and S.H. especially appreciate the support of the US Office of Naval Research, grant N00014-20-1-2517 (to S.W.B.). C.K.B. and C.H.H. gratefully acknowledge support from the Research Corporation for Science Advancement (Cottrell Award). The authors are especially grateful to Shannon W. Boettcher, Hayden Moses, and Jessica Lohrman for their invaluable discussions and technical support. They acknowledge the use of shared instrumentation in the Center for Advanced Materials Characterization in Oregon (CAMCOR) and the Phil and Penny Knight Campus for Accelerating Scientific Impact.

■ REFERENCES

(1) Krämer, J.; et al. Molecular Probes, Chemosensors, and Nanosensors for Optical Detection of Biorelevant Molecules and Ions in Aqueous Media and Biofluids. *Chem. Rev.* **2022**, *122*, 3459−3636.

(2) Cao, R.; et al. Aromatic pentaamide macrocycles bind anions with high affinity for transport across biomembranes. *Nat.Chem.* **2023**, *15*, 1559−1568.
(3) Mefford, J. T.; et al. Correlative operando microscopy of oxygen evolution electrocatalysts. *Nature* **2021**, *593*, 67−73.
(4) Sood, A.; et al. Electrochemical ion insertion from the atomic to the device scale. *Nat. Rev. Mater.* **2021**, *6*, 847−867.
(5) Fleischmann, S.; et al. Pseudocapacitance: From Fundamental Understanding to High Power Energy Storage Materials. *Chem. Rev.* **2020**, *120*, 6738−6782.
(6) He, B.; et al. Halogen chemistry of solid electrolytes in all-solid-state batteries. *Nat. Rev. Chem.* **2023**, *7*, 826−842.
(7) Oener, S. Z.; Foster, M. J.; Boettcher, S. W. Accelerating water dissociation in bipolar membranes and for electrocatalysis. *Science* **2020**, *369*, 1099−1103.
(8) Johnson, D. W.; Cole, D. W. Anion mobility in soils: Relevance to nutrient transport from forest ecosystems. *Environ. Int.* **1980**, *3*, 79−90.
(9) Ryan, P.; Delhaize, E.; Jones, D. Function and mechanism of organic anion exudation from plant roots. *Annu. Rev. Plant Physiol Plant Mol. Biol.* **2001**, *52*, 527−560.
(10) Singh, R. P.; Abbas, N. M.; Smesko, S. A. Suppressed ion chromatographic analysis of anions in environmental waters containing high salt concentrations. *J. Chromatogr A* **1996**, *733*, 73−91.
(11) Powlson, D. S.; et al. When Does Nitrate Become a Risk for Humans? *J. Environ. Qual* **2008**, *37*, 291−295.
(12) Nolan, B. T.; Ruddy, B. C.; Hitt, K. J.; Helsel, D. R. Risk of Nitrate in Groundwaters of the United StatesA National Perspective. *Environ. Sci. Technol.* **1997**, *31*, 2229−2236.
(13) Singh, S.; et al. Nitrates in the environment: A critical review of their distribution, sensing techniques, ecological effects and remediation. *Chemosphere* **2022**, *287*, 131996.
(14) Srinivasan, A.; Viraraghavan, T. Perchlorate: Health Effects and Technologies for Its Removal from Water Resources. *Int. J. Environ. Res. Public Health* **2009**, *6*, 1418−1442.
(15) Steinmaus, C. M. Perchlorate in Water Supplies: Sources, Exposures, and Health Effects. *Curr. Environ. Health Rep* **2016**, *3*, 136−143.
(16) Urbansky, E. T. Perchlorate as an environmental contaminant. *Environmental Science and Pollution Research* **2002**, *9*, 187−192.
(17) Busschaert, N.; Caltagirone, C.; Van Rossom, W.; Gale, P. A. Applications of Supramolecular Anion Recognition. *Chem. Rev.* **2015**, *115*, 8038−8155.
(18) De Marco, R.; Clarke, G.; Pejcic, B. Ion-Selective Electrode Potentiometry in Environmental Analysis. *Electroanalysis* **2007**, *19*, 1987−2001.
(19) Wu, D.; et al. Fluorescent chemosensors: the past, present and future. *Chem. Soc. Rev.* **2017**, *46*, 7105−7123.
(20) Hein, R.; Beer, P. D.; Davis, J. J. Electrochemical Anion Sensing: Supramolecular Approaches. *Chem. Rev.* **2020**, *120*, 1888−1935.
(21) Chen, L.; Berry, S. N.; Wu, X.; Howe, E. N. W.; Gale, P. A. Advances in Anion Receptor Chemistry. *Chem.* **2020**, *6*, 61−141.
(22) Boulas, P. L.; Gómez-Kaifer, M.; Echegoyen, L. Electrochemistry of Supramolecular Systems. *Angew. Chem., Int. Ed.* **1998**, *37*, 216−247.
(23) Beer, P. D.; Gale, P. A. Anion Recognition and Sensing: The State of the Art and Future Perspectives. *Angew. Chem., Int. Ed.* **2001**, *40*, 486−516.
(24) Zhou, H. C.; Long, J. R.; Yaghi, O. M. Introduction to metal-organic frameworks. *Chem. Rev.* **2012**, *112*, 673−674.
(25) Furukawa, H.; Cordova, K. E.; O'Keeffe, M.; Yaghi, O. M. The chemistry and applications of metal-organic frameworks. *Science* **2013**, *341*, 1230444.
(26) Cai, G.; Yan, P.; Zhang, L.; Zhou, H. C.; Jiang, H. L. Metal-Organic Framework-Based Hierarchically Porous Materials: Synthesis and Applications. *Chem. Rev.* **2021**, *121*, 12278−12326.
(27) Boyd, P. G.; et al. Data-driven design of metal−organic frameworks for wet flue gas CO_2 capture. *Nature* **2019**, *576*, 253−256.
(28) Siegelman, R. L.; Kim, E. J.; Long, J. R. Porous materials for carbon dioxide separations. *Nat. Mater.* **2021**, *20*, 1060−1072.
(29) Lin, J. B.; et al. A scalable metal-organic framework as a durable physisorbent for carbon dioxide capture. *Science* **2021**, *374*, 1464−1469.
(30) Kim, E. J.; et al. Cooperative carbon capture and steam regeneration with tetraamine-appended metal−organic frameworks. *Science* **2020**, *369*, 392−396.
(31) Islamoglu, T.; et al. Metal−Organic Frameworks against Toxic Chemicals. *Chem. Rev.* **2020**, *120*, 8130−8160.
(32) Yang, S.; et al. Supramolecular binding and separation of hydrocarbons within a functionalized porous metal−organic framework. *Nat. Chem.* **2015**, *7*, 121−129.
(33) Chen, K. J.; et al. Synergistic sorbent separation for one-step ethylene purification from a four-component mixture. *Science* **2019**, *366*, 241−246.
(34) Datta, S. J.; et al. Rational design of mixed-matrix metal-organic framework membranes for molecular separations. *Science* **2022**, *376*, 1080−1087.
(35) Baumann, A. E.; Burns, D. A.; Liu, B.; Thoi, V. S. Metal-organic framework functionalization and design strategies for advanced electrochemical energy storage devices. *Commun. Chem.* **2019**, *2*, 86.
(36) Chen, K.; et al. $Cu[Ni(2,3\text{-pyrazinedithiolate})_2]$ Metal-Organic Framework for Electrocatalytic Hydrogen Evolution. *ACS Appl. Mater. Interfaces* **2021**, *13*, 34419−34427.
(37) Johnson, B. A.; Beiler, A. M.; McCarthy, B. D.; Ott, S. Transport Phenomena: Challenges and Opportunities for Molecular Catalysis in Metal-Organic Frameworks. *J. Am. Chem. Soc.* **2020**, *142*, 11941−11956.
(38) Castner, A. T.; et al. Microscopic Insights into Cation-Coupled Electron Hopping Transport in a Metal-Organic Framework. *J. Am. Chem. Soc.* **2022**, *144*, 5910−5920.
(39) Cai, M.; Loague, Q.; Morris, A. J. Design Rules for Efficient Charge Transfer in Metal-Organic Framework Films: The Pore Size Effect. *J. Phys. Chem. Lett.* **2020**, *11*, 702−709.
(40) Lin, H.; et al. Metal−Organic Frameworks for Water Harvesting and Concurrent Carbon Capture: A Review for Hygroscopic Materials. *Adv. Mater.* **2024**, *36*, 2209073.
(41) Çamur, C.; et al. Monolithic Zirconium-Based Metal−Organic Frameworks for Energy-Efficient Water Adsorption Applications. *Adv. Mater.* **2023**, *35*, 2209104.
(42) Xie, L. S.; Skorupskii, G.; Dincă, M. Electrically Conductive Metal-Organic Frameworks. *Chem. Rev.* **2020**, *120*, 8536−8580.
(43) Campbell, M. G.; Liu, S. F.; Swager, T. M.; Dincă, M. Chemiresistive Sensor Arrays from Conductive 2D Metal−Organic Frameworks. *J. Am. Chem. Soc.* **2015**, *137*, 13780−13783.
(44) Meng, Z.; Stolz, R. M.; Mirica, K. A. Two-Dimensional Chemiresistive Covalent Organic Framework with High Intrinsic Conductivity. *J. Am. Chem. Soc.* **2019**, *141*, 11929−11937.
(45) Aykanat, A.; Meng, Z.; Stolz, R. M.; Morrell, C. T.; Mirica, K. A. Bimetallic Two-Dimensional Metal−Organic Frameworks for the Chemiresistive Detection of Carbon Monoxide. *Angew. Chem., Int. Ed.* **2022**, *61*, No. e202113665.
(46) Gamonal, A.; et al. Divergent Adsorption-Dependent Luminescence of Amino-Functionalized Lanthanide Metal−Organic Frameworks for Highly Sensitive NO_2 Sensors. *J. Phys. Chem. Lett.* **2020**, *11*, 3362−3368.
(47) Kreno, L. E.; et al. Metal-organic framework materials as chemical sensors. *Chem. Rev.* **2012**, *112*, 1105−1125.
(48) Shustova, N. B.; Cozzolino, A. F.; Reineke, S.; Baldo, M.; Dincă, M. Selective Turn-On Ammonia Sensing Enabled by High-Temperature Fluorescence in Metal−Organic Frameworks with Open Metal Sites. *J. Am. Chem. Soc.* **2013**, *135*, 13326−13329.
(49) Dolgopolova, E. A.; Rice, A. M.; Martin, C. R.; Shustova, N. B. Photochemistry and photophysics of MOFs: steps towards MOF-based sensing enhancements. *Chem. Soc. Rev.* **2018**, *47*, 4710−4728.

https://doi.org/10.1021/jacs.4c06669
J. Am. Chem. Soc. XXXX, XXX, XXX−XXX

(50) Feng, Y.; Wang, Y.; Ying, Y. Structural design of metal−organic frameworks with tunable colorimetric responses for visual sensing applications. *Coord. Chem. Rev.* **2021**, *446*, 214102.
(51) Ko, M.; et al. Employing Conductive Metal−Organic Frameworks for Voltammetric Detection of Neurochemicals. *J. Am. Chem. Soc.* **2020**, *142*, 11717−11733.
(52) Huang, J.; et al. Giant Redox Entropy in the Intercalation vs Surface Chemistry of Nanocrystal Frameworks with Confined Pores. *J. Am. Chem. Soc.* **2023**, *145*, 6257−6269.
(53) Marshall, C. R.; et al. Size-Dependent Properties of Solution-Processable Conductive MOF Nanocrystals. *J. Am. Chem. Soc.* **2022**, *144*, 5784−5794.
(54) Park, J. G.; et al. Charge Delocalization and Bulk Electronic Conductivity in the Mixed-Valence Metal-Organic Framework $Fe(1,2,3\text{-triazolate})_2(BF_4)_x$. *J. Am. Chem. Soc.* **2018**, *140*, 8526−8534.
(55) Park, J. G.; et al. Magnetic ordering through itinerant ferromagnetism in a metal−organic framework. *Nat. Chem.* **2021**, *13*, 594−598.
(56) Gándara, F.; et al. Porous, conductive metal-triazolates and their structural elucidation by the charge-flipping method. *Chemistry A European J* **2012**, *18*, 10595−10601.
(57) Mitchell, J. B.; Wang, R.; Ko, J. S.; Long, J. W.; Augustyn, V. Critical Role of Structural Water for Enhanced Li^+ Insertion Kinetics in Crystalline Tungsten Oxides. *J. Electrochem. Soc.* **2022**, *169*, 030534.
(58) Tsai, W. Y.; Taberna, P. L.; Simon, P. Electrochemical quartz crystal microbalance (EQCM) study of ion dynamics in nanoporous carbons. *J. Am. Chem. Soc.* **2014**, *136*, 8722−8728.
(59) Levi, M. D.; et al. Solving the capacitive paradox of 2D MXene using electrochemical quartz-crystal admittance and in situ electronic conductance measurements. *Adv. Energy Mater.* **2015**, *5*, 1400815.
(60) Andreeva, A. B.; et al. Cooperativity and Metal−Linker Dynamics in Spin Crossover Framework $Fe(1,2,3\text{-triazolate})_2$. *Chem. Mater.* **2021**, *33*, 8534−8545.
(61) Andreeva, A. B.; et al. Soft Mode Metal-Linker Dynamics in Carboxylate MOFs Evidenced by Variable-Temperature Infrared Spectroscopy. *J. Am. Chem. Soc.* **2020**, *142*, 19291−19299.

https://doi.org/10.1021/jacs.4c06669
J. Am. Chem. Soc. XXXX, XXX, XXX−XXX